

## Research Article

# A New Measurement Based on HPB to Measure the Wall Pressure of Electric-Spark-Generated Bubble near the Hemispheric Boundary

Chunlong Ma <sup>1,2</sup>, Dongyan Shi <sup>1</sup>, Xiongwei Cui <sup>3</sup>, and Yingyu Chen <sup>3</sup>

<sup>1</sup>College of Mechanical and Electrical Engineering, Harbin Engineering University, Harbin, China

<sup>2</sup>Harbin Vocational & Technical College, Harbin, China

<sup>3</sup>College of Shipbuilding Engineering, Harbin Engineering University, Harbin, China

Correspondence should be addressed to Dongyan Shi; [shidongyan@hrbeu.edu.cn](mailto:shidongyan@hrbeu.edu.cn)

Received 13 June 2019; Revised 20 August 2019; Accepted 12 December 2019; Published 10 February 2020

Academic Editor: Chao Tao

Copyright © 2020 Chunlong Ma et al. This is an open access article distributed under the Creative Commons Attribution License, which permits unrestricted use, distribution, and reproduction in any medium, provided the original work is properly cited.

Direct measurement of the wall pressure loading of the spherical boundary subjected to the near-field underwater explosion is a great difficulty. To investigate the wall pressure caused by electric-spark-generated bubble near a hemispheric boundary, an experiment system is developed. In the method of this experiment, a Hopkinson bar (HPB), used as the sensing element, is inserted through the hole drilled on the hemisphere target and the bar's measuring end face lies flush with the loaded face of the hemisphere target to detect and record the pressure loading. The semiconductor strain gauges which stick on Hopkinson bar are used to convert the pressure-based signal to the strain wave signal. The bubble in the experiments is formed by a discharge of 400 V high voltage. To validate the pressure measurement technique based on the HPB, an experimental result from pressure transducer is used as the validating system. To verify the capability of this new methodology and experimental system, a series of electric-spark-generated bubble experiments are conducted. From the recorded pressure-time profiles coupled with the underwater explosion evolution images captured by the high-speed camera (HSV), the shock wave pressure loading and bubble collapse pressure loadings are captured in detail at different dimensionless stand-off distances  $\gamma$  from 0.17 to 2.00. From the results of the experiments conducted in this paper, the proposed experiment system can be used to measure the pressure signal successfully, giving new way to study the bubble collapse pressure when the bubble is near a hemispheric boundary. Through the experimental results, the bubbles generated by different dimensionless stand-off distance  $\gamma$  are divided into four categories, and the bubble load characteristics are also discussed.

## 1. Introduction

The cavitation bubbles exist widely in nature. Mainly, they experience three different stages: expansion, contraction, or shrinking and collapse [1, 2]. When the collapse of a bubble occurs near a structure, the structure will bear an impact due to the collapsing bubble [3]. At the same time, high-speed liquid jets can also occur in the final stage of bubble collapse [4, 5]. Therefore, the damage characteristics of bubbles to adjacent structures are critical in fluid mechanics. The study of the characteristics of the interaction between the bubble and the nearby structure has become the focus of many technical fields, for example, cavitation erosion of nearby

structure [6, 7], underwater explosion [8], and ultrasonic cleaning [5].

To study the bubble dynamics and the pressure mechanics of the adjacent structures, a lot of work has been carried out on laser-generated or electric-spark-generated bubbles near a solid planar boundary. Tong et al. [9] experimentally observed the effect of distance from a solid planar boundary on bubble collapse for laser-generated bubble and obtained the wall pressure by using pressure transducers. By using the pressure transducer, the spark-generated bubble dynamics and the pressure curves on the solid planar boundary center at different distances have also been discussed. As a new measurement, by using Hopkinson

bar, Cui et al. [10] investigated the pressure characteristics of microcharge bubble on the solid planar boundary from experimental aspects. If it is assumed that the fluid field surrounded the bubble and the boundary is inviscid, incompressible, and irrotational, the boundary integral method can be an effective way to simulate the bubble dynamics near rigid boundaries [11–14]. Tomita et al.'s work [15] from both a numerical and experimental perspective was to elucidate the effect of the surface curvature of the boundary on the bubble dynamics. It is shown that the curvature of the rigid boundary can significantly influence the collapse of a nearby laser-generated bubble. For the boundary with curvature, the oscillation features of the UNDEX bubble near a bilge with a circle opening are studied experimentally under the help of electric-spark-generated bubbles and HSV [16]. Li et al. [17–19] combined the bubble-structure interaction model of the fully coupled model to study the bubble-sphere interaction near the free surface and proposed a three-dimensional model of the interaction between the ball and the nearly hemispherical bubble attached to the surface of the sphere. According to the studies given above, it can be found that the study of the pressure loading by cavitation bubble near the curved boundary generated is considerably rare. There is no doubt that the geometry and curvature of the boundary play an extremely important role in the expansion, contraction, and collapse of the bubble, subsequently affecting the characteristics of the pressure loading.

Using a Hopkinson bar to measure pressure loading has been successfully applied to detect the pressure of shock wave on the target plate subjected to air blast, explosions buried in the dry sand [20–22]. For underwater explosion, the pressure loading is more complex. After the explosion, an extremely strong shock wave is generated and massive bubble is released. Then a high-pressure underwater explosion bubble begins to expand and then shrink. Due to the factors of Bjerknes effect, inertia, and gravity, a water jet can be formed. Then the water jet will impact on the nearby structure. When the bubble shrinks to its minimal volume, it will emit another shock wave in water. To obtain a series of continuous separate loadings, Yao et al. [23, 24] proposed a new pressure measuring methodology to measure the pressure loading on the rigid plate due to the high-voltage electric-spark-generated bubble. To meet the requirements of the underwater operation conditions, all the key elements of the test system are enclosed in a waterproof enclosure.

Based on Yao et al.'s [23, 24] work, we change the shape of the target to study the pressure loading on the hemispheric boundary generated by the electric-spark-generated bubble. As an efficient way, the electric-spark-generated bubble [25–30] is used to study the underwater bubble dynamics for its low cost. In this paper, we firstly use a new measurement based on HPB to measure wall pressure to investigate the wall pressure generated beneath the hemispheric boundary. We use experimental methods to study the bubble dynamics and pressure mechanics of electric-spark-generated bubbles near the hemisphere boundary. The bubble collapse pressure loadings are related to the bubble dynamics. A high-speed camera (HSV) is used to capture the images of the bubble's motion. HPB is used to measure the

wall pressure load caused by electric spark bubbles. The joint analysis of the pressure loading measured by the Hopkinson bar and the bubble dynamics captured by the high-speed camera is carried out.

## 2. Experimental System and Measurement Method

*2.1. Experimental System.* To investigate the wall pressure on the hemispheric boundary caused by an underwater electric spark bubble, an experimental setup using a HPB as the sensing element is designed. The detailed schematic of the experimental equipment is shown in Figure 1. The hemispheric target is mounted to the waterproof tube by threaded connection. At the center of hemispheric target a through-hole is drilled through which the HPB is inserted. With the help of several seal rings, the waterproof tube and the hemispheric target constitute a waterproof enclosure. The diameter of the hemispheric target is 50 mm.

In this experiment, the material of HPB is steel. The length and the diameter of HPB are 2.3 m and 5 mm, respectively. Based on the stress wave theory, the pressure loading can be obtained according to the stress-strain relation. The semiconductor strain gauges are pasting at the point which is 0.1 m from measuring end of HPB to record the signal which is in HPB. The experiment uses opposite double strain gauges and pastes the double strain gauges on the same round section of HPB. A Wheatstone-bridge circuit is used to transfer the resistance signal generated by the strain gauge to the voltage signal.

The experimental system schematic is shown in Figure 2. The water tank used in this experiment is 600 mm long, 600 mm wide, and 600 mm high. The water depth of the water tank is 525 mm, and the bottom of hemispheric target is 390 mm higher than the bottom of the water tank. The electric-spark-generated bubble is an efficient method to study the underwater bubble dynamics for its low cost. In this paper, the underwater bubble is generated by means of underwater electric discharge (400 V). The maximum equivalent bubble radius  $R_m$  is 30 mm. The motion of bubbles near the hemispheric boundary was captured by a high-speed camera at 24000 frames/s.

*2.2. Experimental Parameters.* This section first defines a dimensionless parameter to represent the distance between electric spark explosion source and the bottom of hemispheric target. Based on the spherical hypothesis of shock wave, the dimensionless distance from the initial bubble to the bottom of the hemispheric target is defined as  $\gamma = d/2R_m$ . The dimensionless stand-off distance  $\gamma$  is a predominant factor in determining the effects of a nearby boundary on bubble.  $R_m$  is the maximum radius of the electric-spark-generated bubble. The maximum radius of the bubble in a free field is about 30 mm, which is obtained from images captured by HSV; the details are shown in Figure 3.  $d$  is the straight line distance between the detonation point and the bottom of the hemispheric boundary, where the shock wave first reaches. More details are shown in Figure 4.

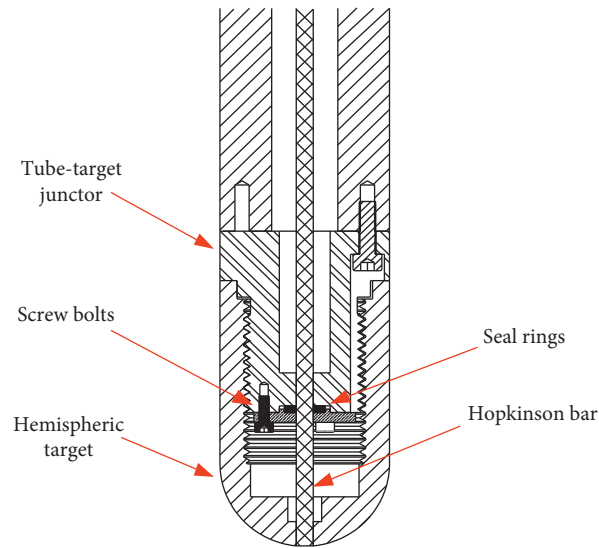


FIGURE 1: Detailed schematic of the apparatus.

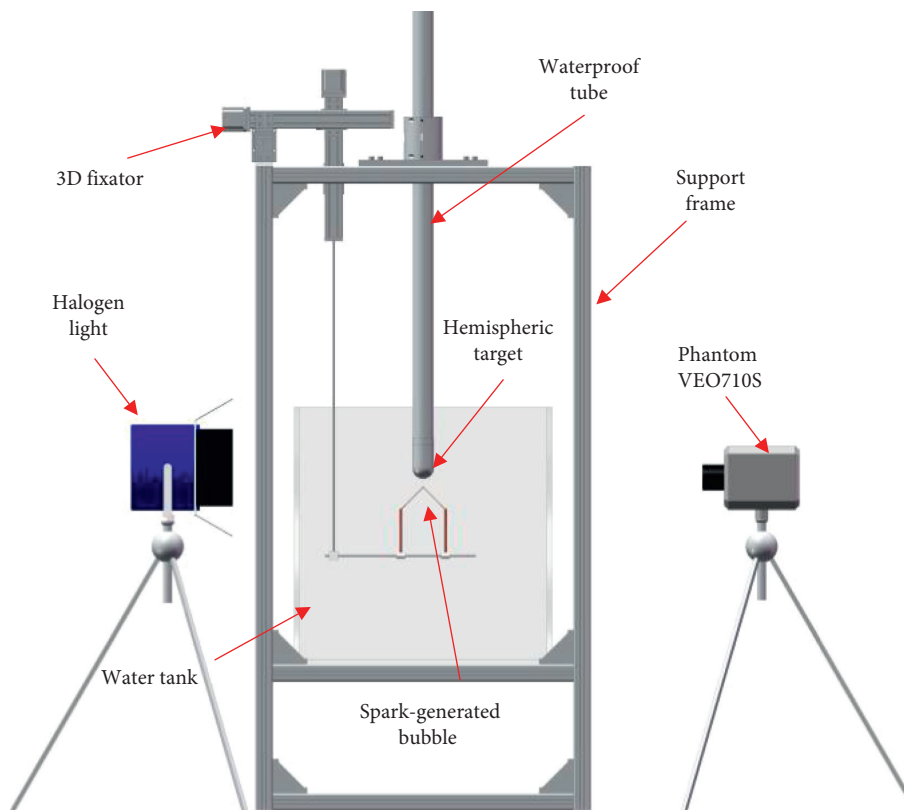


FIGURE 2: Experimental system schematic.

### 2.3. Data Analysis Method and Validation

**2.3.1. Stress Wave in HPB.** The stress wave generated by the underwater explosion propagates to the distal end of the Hopkinson bar and then reflects back; the reflected stress wave propagates to the position of the strain gauge on the Hopkinson bar; strain gauge will record reflected wave strain signal. That is, the maximum pulse width of the wall pressure

that the Hopkinson bar can measure is the time quantum ( $\Delta T$ ) where the incident stress wave passes through the distal end of the Hopkinson bar and the reflection propagates to the strain gauge. When Hopkinson bar length is constant, the interval time quantum ( $\Delta T$ ) between the occurrence time of the stress wave strain signal generated from the wall pressure and the occurrence time of the reflected stress wave strain signal is

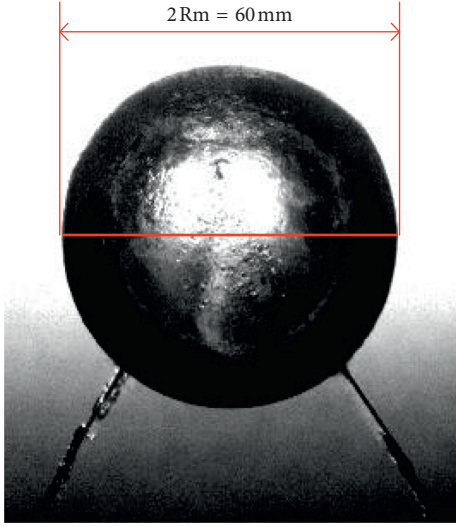


FIGURE 3: Maximum radius of the bubble is about 30 mm by a discharge of 400 V in a free field.

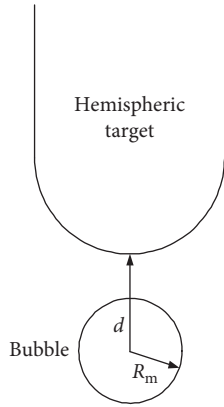


FIGURE 4: Schematic diagram of related physical quantities in a dimensionless definition.

$$\Delta T = \frac{2 \times D_{\text{Distal}}}{C_0} \quad (1)$$

Distance from the far end of the measuring point is  $D_{\text{Distal}}$ . Velocity of stress waves in Hopkinson bar is  $C_0$ .

According to the above analysis, in the future, the strain signal of the measuring bar will appear as a mixed signal of stress waves and reflected waves, which is no longer the wall pressure signal itself. On the one hand, when wall pressure period  $T_{\text{Pressure}}$  is greater than  $\Delta T$ , the measured stress wave signal will be a mixed signal of the reflected stress wave signal and the next input wall pressure signal, which means wall pressure measurement failed. That is, for Hopkinson bar of a certain length, the measurable wall pressure period  $T_{\text{Pressure}}$  needs to be met:

$$T_{\text{Pressure}} \leq \Delta T = \frac{2 \times D_{\text{Distal}}}{C_0} \quad (2)$$

On the other hand, for wall pressure signals that meet the above requirements, in this paper, we removed the reflected wave signal to obtain a legible signal.

The length of Hopkinson bar used in this study is 2.3 m, the distance between strain gauge and measurement end is 0.1 m, and the propagation velocity of stress wave in Hopkinson bar is 4.98 km/s; that is,  $\Delta T = 0.884$  ms. Therefore, the maximum pulse width of the wall pressure that the Hopkinson rod used in this study can measure is 0.884 ms. In this study, the pulse width range ( $\theta_{c1}$ ) of the first period bubble collapse is  $0 \text{ ms} \leq \theta_{c1} \leq 0.15 \text{ ms}$  (details are shown in Figure 5). The pulse width range ( $\theta_{c2}$ ) of the second period bubble collapse is  $0 \text{ ms} \leq \theta_{c2} \leq 0.15 \text{ ms}$  (details are shown in Figure 6). Because  $\theta_{c1}$  and  $\theta_{c2}$  are both less than  $\Delta T$ , the bubble collapse load measured in this paper is effective, which is not affected by reflected waves.

We explain the feasibility of the system to measure wall pressure load from another aspect right now. The pressure-time diagram generated by the electric spark bubble collapse during the first cycle is shown in Figure 7. The first collapse of bubble began with  $t_1 = 5.968$  ms, and reflected wave signals were detected at  $t_2 = 6.853$  ms. The Hopkinson bar used in this experiment is 2.3 m long and the strain gauges are pasted at a distance of 0.1 m from the measuring end of Hopkinson bar, which means the propagation velocity of the stress wave in the Hopkinson bar is about 4.98 km/s. The stress wave is detected by strain gauges for the first time at  $t_1 = 5.968$  ms. At  $t_2 = 6.853$  ms, the reflected wave is detected for the first time by the strain gauge. At  $t_3 = 6.925$  ms, the reflected wave is detected for the second time by the strain gauge. At  $t_4 = 7.808$  ms, the reflected wave is detected for the third time by the strain gauge. In this way, the situation is the same as above. At  $t_5 = 7.882$  ms, the reflected wave is detected for the fourth time by the strain gauge. At  $t_6 = 8.767$  ms, the reflected wave is detected for the fifth time by the strain gauge. At  $t_7 = 8.840$  ms, the reflected wave is detected for the sixth time by the strain gauge. The absolute of the reflected wave detected by the strain gauge decreases gradually.

During the first bubble collapse, the acquisition times of the initial stress wave and reflection stress wave detected by the strain gauges are shown in Table 1. Combining the analyses of Figure 7 and Table 1, we can easily find that the time when the strain gauge detects the shock wave of the second period of bubble collapse and the time of detecting the reflected wave of the first period of the bubble are different. So it is feasible to measure the wall pressure of spark-generated bubble by Hopkinson bar.

According to the above analysis, in order to simplify the pressure-time diagram and highlight the peak characteristics of bubble collapse to be discussed in this study, in the following discussion, we only show the bubble collapse stress waves detected by the strain gauge, as shown in Figure 8.

The strain gauges stick on the Hopkinson bar used in the experiment are semiconductor strain gauges and the sensitivity  $S_{\text{Gauge}}$  is 110.  $U_{\text{Bridge}}$  supply voltage of the ultra-dynamic strain gauge is 2 VDC. The relationship between the strain  $\varepsilon_H$  of Hopkinson bar and the output voltage signal  $U_c$  of super dynamic strain gauge is

$$\varepsilon_H = \frac{U_c \times F_{\text{Bridge}} \times U_{\text{Bridge}} \times 1000}{S_{\text{Gauge}}} (\mu\varepsilon), \quad (3)$$

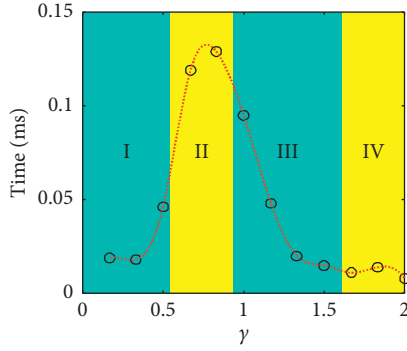


FIGURE 5: The pulse width data of the bubble load in the first cycle variation diagram for  $0.17 \leq \gamma \leq 2.00$ .

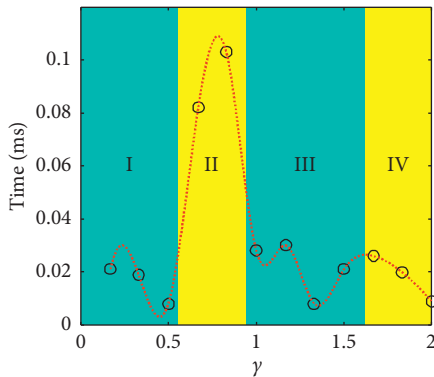


FIGURE 6: The pulse width data of the bubble load in the second cycle variation diagram for  $0.17 \leq \gamma \leq 2.00$ .

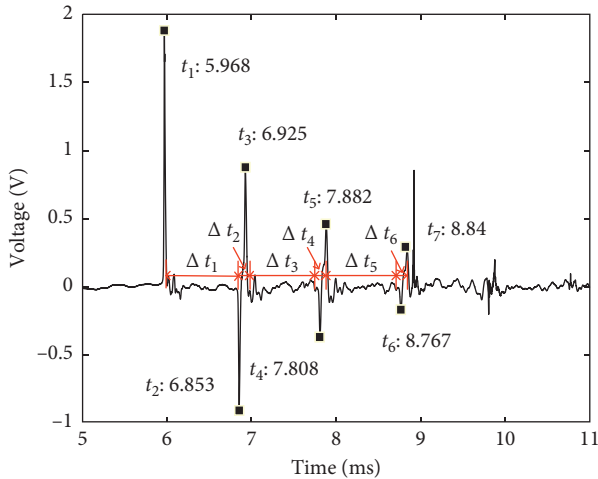


FIGURE 7: Voltage-time diagram of stress waves and reflected waves detected by strain gauges.

where  $F_{\text{Bridge}}$  is the bridge variable coefficient. In this experiment, double strain gauge bridge is adopted, and its bridge variable coefficient is  $F_{\text{Bridge}} = 1/2$ .

According to the material mechanical properties of Hopkinson bar,  $E_p$  is the elastic modulus; then the Pressure<sub>Hop</sub> wall pressure on the target plate can be obtained according to the following formula. The image of wall

pressure load converted from measured electrical signals is shown in Figure 9.

$$\text{Pressure}_{\text{Hop}} = \frac{E_p \times \varepsilon_H = E_p \times U_c \times F_{\text{Bridge}} \times U_{\text{Bridge}}}{S_{\text{Gauge}} \times 1} \text{ (MPa)}. \quad (4)$$

**2.3.2. Validation.** Because the Hopkinson bar is a new measurement used to measure the wall pressure load produced by electric-spark-generated bubble, the authenticity of the data measured by Hopkinson bar remains to be validated. The pressure transducer and HPB are used to measure the wall pressure load caused by the electric spark bubbles under the same working conditions, and the measurement performance of HPB is verified by comparing their measurement results. The pressure transducer used in the verification experiments is a piezoelectric pressure transducer produced by SINOCERA PIEZOTRONICS INC, just as shown in Figure 10. And another production of the same company YE5853 is adopted as the charge amplifier. The pressure transducer is model 37311. The maximum measured pressure of the pressure transducer used is 60 MPa. Its sensitivity coefficient is 13.68 mV/Pa.

As shown in Figure 11 and 12, the wall pressure load data measured by the Hopkinson bar are almost the same as those measured by the pressure transducer in cases of  $\gamma = 0.33$  and 0.67. Therefore, it can be determined that the wall pressure load measured by Hopkinson bar is equivalent to the actual wall pressure load by electric-spark-generated bubble. However, the wall pressure sensor cannot measure the wall pressure load in the near field, while HPB can, which is the key to this measurement technology.

In Table 2, the relative errors between HPB and pressure transducer's peak pressure are given. The relative errors are less than 2%. From the results, it can be concluded that the peak pressures of the wall pressure measured by the Hopkinson bar and the pressure transducer are almost the same. Moreover, it can also be seen from Figures 11 and 12 that the shapes of the pressure curves and pressure pulse widths are also approximately the same. Moreover, the effectiveness of the parallel principle system based on the same Hopkinson bar has also been discussed in Cui et al.'s [10] work.

### 3. Bubble Dynamics and Load Characteristics under Different $\gamma$

To validate and investigate the capability of the new measured methodology and experimental system to measure the wall pressure loading near the hemispherical boundary, a series of electric-spark-generated bubble experiments are conducted. The explosion source used in the experiments is the high voltage of 400 V. This series of experiments was performed under a hemispherical target. From the above, the maximum diameter of the electric spark bubble generated at the 400 V discharge point is 60 mm. In this study, 12 groups of experiments were performed according to the constant increase of the dimensionless constant  $\gamma$  (0.17, 0.33, ..., 2.00), and the 12 groups of experiments were divided into 4

TABLE 1: Acquisition time of initial stress wave and stress reflection wave in the first collapse of bubbles: ① 1<sup>st</sup> IW is the time of first incident wave signal; ② 1<sup>st</sup> RW is the time of the first reflected wave signal; ③ 2<sup>nd</sup> RW is the time of the second reflected wave signal; ④ 3<sup>rd</sup> RW, 4<sup>th</sup> RW, and so on are the same as before.

	1 <sup>st</sup> IW ( $t_1$ )	1 <sup>st</sup> RW ( $t_2$ )	2 <sup>nd</sup> RW ( $t_3$ )	3 <sup>rd</sup> RW ( $t_4$ )	4 <sup>th</sup> RW ( $t_5$ )	5 <sup>th</sup> RW ( $t_6$ )	6 <sup>th</sup> RW ( $t_7$ )
$t$ (ms)	5.968	6.852	6.925	7.808	7.882	8.766	8.839
$\Delta t$ (ms)	—	$\Delta t_1$	$\Delta t_2$	$\Delta t_3$	$\Delta t_4$	$\Delta t_5$	$\Delta t_6$
		0.884	0.073	0.883	0.074	0.884	0.073

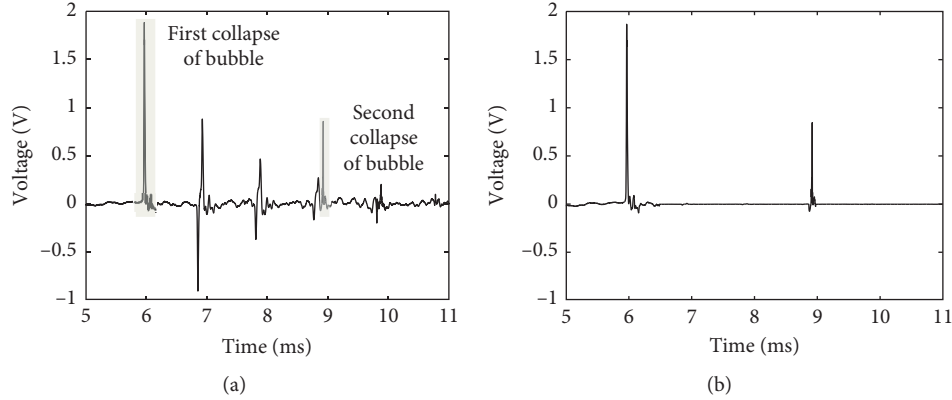


FIGURE 8: Data analysis in this paper. (a) The original signal. (b) Stress waves of bubble collapse only.

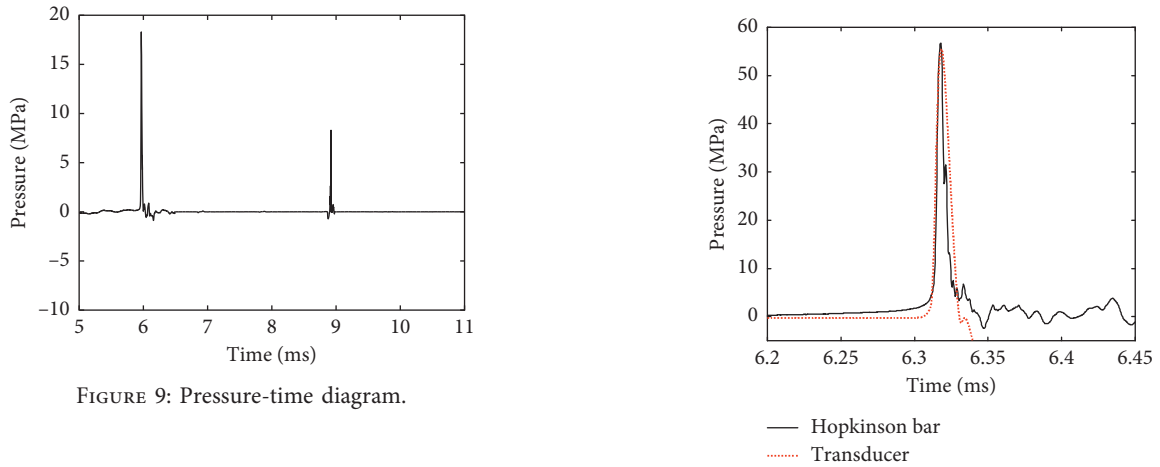


FIGURE 9: Pressure-time diagram.

FIGURE 11:  $\gamma = 0.33$ ; Hopkinson bar measured data and transducer measured data comparison.

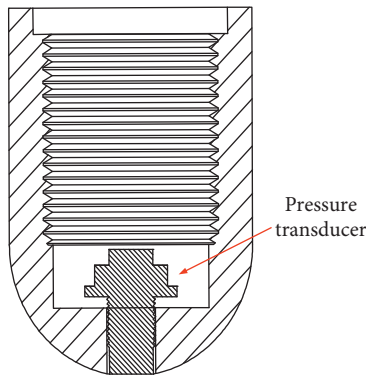


FIGURE 10: Pressure transducer on the hemispheric target.

categories according to the experimental results, as shown in Table 3. The wall pressure-time curves corresponding to different dimensionless constants  $\gamma$  are given in Appendix.

**3.1. Inverted Mushroom-Like Bubble (Type I).** When  $\gamma = 0.33$ , the dynamic change process of the specific bubble is shown in Figure 13. As we can see from the figure, at  $t = 0$  ms, the intersection of the copper tube emits strong light and begins to form a bubble. At  $t = 0.833$  ms, with the expansion of bubble, the upper end of the bubble is connected to the hemispheric target, and, with the passage of time, the upper end of the bubble is further expanded around the hemispheric target surface, and the bottom of the bubble is still kept spherical. At  $t = 3.499$  ms, the bubble expands to the maximum volume in the first cycle, and the bubble is already completely wrapped around the hemispheric target. With the bubble shrinking, at  $t = 5.832$  ms, the bubble is shaped like an inverted mushroom due to the acceleration of bubble

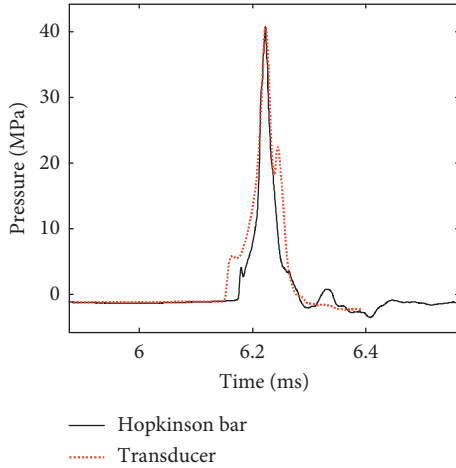


FIGURE 12:  $\gamma = 0.67$ ; Hopkinson bar measured data and transducer measured data comparison.

TABLE 2: The relative errors of peak pressure between the Hopkinson bar and pressure transducer.

	$\gamma = 0.33$	$\gamma = 0.67$
Hopkinson bar (MPa)	56.702	42.294
Pressure transducer (MPa)	55.597	41.575
Relative error (%)	1.9	1.7

TABLE 3: Experimental cases.

Test	Voltage	Boundary condition	$\gamma$	Type
1			0.17	
2			0.33	I
3			0.50	
4			0.67	II
5			0.83	
6	400 V	Under the hemisphere target	1.00	
7			1.17	III
8			1.33	
9			1.50	
10			1.67	
11			1.83	IV
12			2.00	

shrinkage along the hemispheric target surface. Since the liquid flows inward along the boundary of the curved surface, the “mushroom” head of the bubble is pushed up from below, causing the neck of the mushroom-like bubble to elongate. At  $t = 6.207$  ms, the characteristics of inverted mushroom-like bubble are more obvious. As the bubble collapses, the mushroom-like cap becomes flattened and the diameter of mushroom becomes thinner and longer. At  $t = 6.290$  ms, the bubble shrinks to the smallest volume, and it is considered the end time of the first stage of bubble pulsation. At this time, the collapse moment can also be clearly observed, and a downward jet is produced from the center of the bottom of hemispheric target surface. At  $t = 6.540$  ms, the bubble has entered the expansion stage of

the second cycle. Due to the generation of downward jet, the bubble moves downward along the vertical direction. With the passage of time, the upper part of the bubble is wrapped around the surface of hemispheric target, and the lower part of the bubble moves down rapidly. In the end, there is an obvious phenomenon of bubble separation and shedding. At  $t = 7.624$  ms, the bubble expands to the maximum volume state again. At  $t = 8.915$  ms, the upper part of the bubble collapses obviously, and the bubbles fall off completely. At  $t = 9.082$  ms, the upper bubble collapses to the minimum volume.

Hopkinson bar is used to record strain signals and analyze the characteristics of bubble load, as shown in Figure 14. When the bubble collapses in the first stage, the bubble load has bimodal characteristics. When  $t$  is 6.318 ms and 6.321 ms, there are two load peaks. Compared with bubble dynamics diagram in Figure 13 when  $t = 6.290$  ms, it is found that the corresponding load peaks are bubble collapse load  $P_{c-1}$  and water jet load  $P_{j-1}$ , whose peak values are 56.71 MPa and 31.46 MPa, respectively. During the second periodic collapse stage of the bubble, the bubble load also has bimodal characteristics. When  $t$  is 9.132 ms and 9.136 ms, there are load peaks. Compared with bubble dynamics diagram in Figure 13 when  $t = 9.082$  ms, it is found that the corresponding loads are bubble collapse load  $P_{c-2}$  and water jet load  $P_{j-2}$ , whose peak values are 23.15 MPa and 15.49 MPa, respectively. Based on the comparison, it is found that the bubble load duration of the second cycle is obviously longer than that of the first cycle. The peak of bubble load decreases obviously in the second cycle due to bubble shedding.

It is found that when the dimensionless distance parameter  $\gamma$  is between 0.17 and 0.5, it has similar bubble shape and load characteristics. Therefore, in order to facilitate the analysis under different  $\gamma$ , it is divided into inverted mushroom-like bubble as the type I. The major morphological characteristics of inverted mushroom-like bubble can be described as follows: as shown in Figure 15, in the first cycle, the expansion stage of bubbles will be spherical. Due to the influence of boundary conditions, the bubble expands to the maximum volume and surrounds the hemispheric target. In the first cycle of bubble contraction, bubbles shrink in the form of inverted mushroom-like bubble. This type of bubble will induce a water jet act onto the hemisphere target in the collapse stage of the first cycle. At this time, two peak pressures are measured by Hopkinson bar, which are bubble collapse load  $P_{c-1}$  and water jet load  $P_{j-1}$  in the first cycle. In the expansion stage of the second cycle, the bubble expands in the shape of hemispherical shape, and the bubble partially surrounds the hemispheric target. In the shrinking stage of the second cycle, the bubble contracts in the form of inverted cone-like bubble, and the bottom of the cone is connected with the hemispheric target. Bubbles will separate in the collapse stage of the second cycle; one bubble will form a jet acting on the hemispheric target, and the other bubble will separate in the opposite direction of the hemispheric target. At this time, two peak pressures are also measured by Hopkinson bar, which are bubble collapse load  $P_{c-2}$  and water jet load  $P_{j-2}$  in the second cycle. There are two bubble

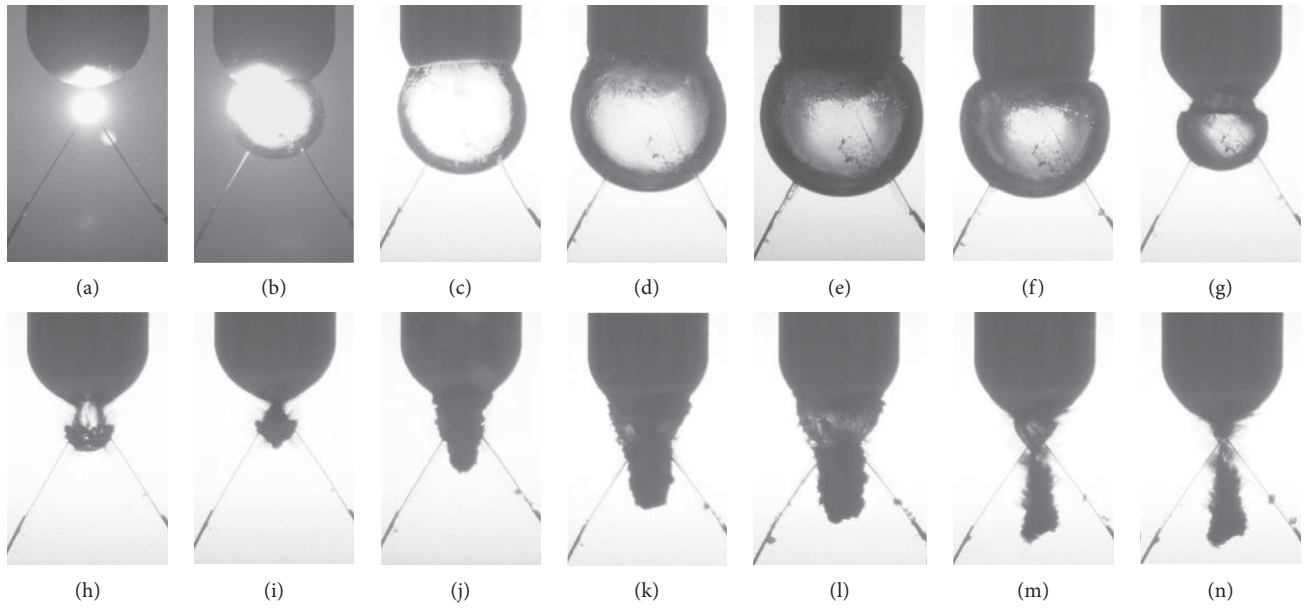


FIGURE 13: Bubble dynamics under the influence of hemispheric boundary for  $\gamma = 0.33$ . (a) 0.000 ms. (b) 0.833 ms. (c) 1.458 ms. (d) 2.583 ms. (e) 3.499 ms. (f) 4.541. (g) 5.832 ms. (h) 5.207 ms (i) 5.290 ms. (j) 6.540 ms. (k) 7.040 ms. (l) 7.624 ms. (m) 8.915 ms. (n) 9.082 ms.

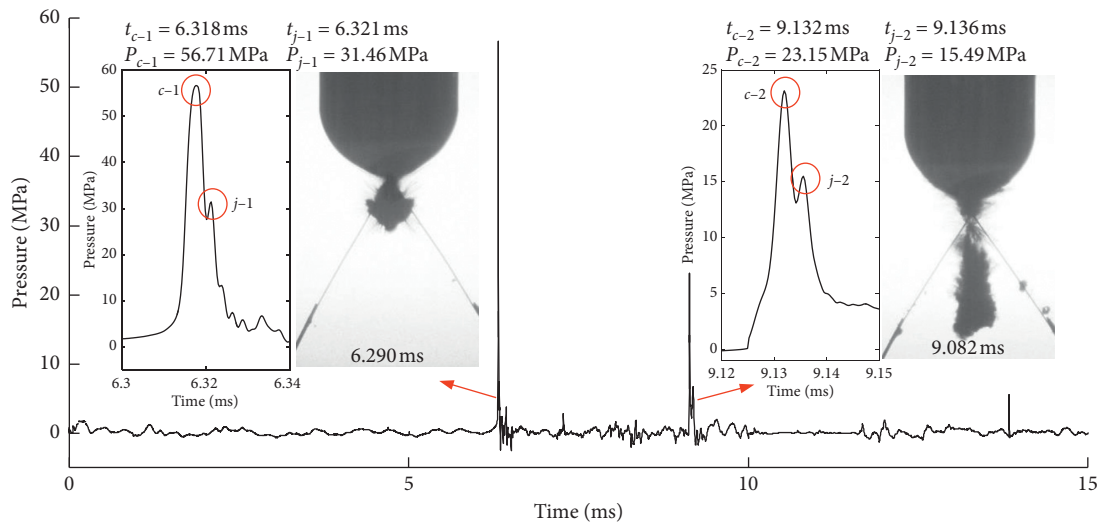


FIGURE 14: Pressure-time diagram of the first and second cycles of the electric-spark-generated bubble load for  $\gamma = 0.33$ .

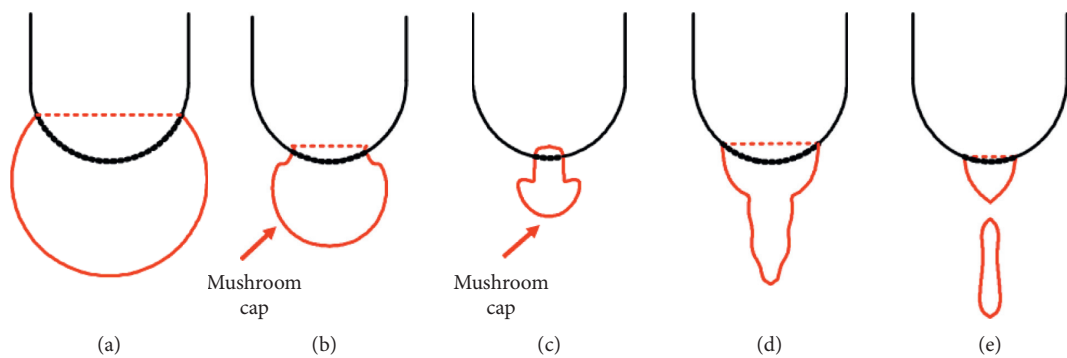


FIGURE 15: Description of morphological characteristics of inverted mushroom-like bubble. (a) First maximum volume. (b) Inverted mushroom. (c) Mushroom-like. (d) Second maximum volume. (e) Second minimum volume.

load peaks in both the first cycle and the second cycle; they are collapse load and jet load.

**3.2. Oval Bubble (Type II).** When  $\gamma=0.67$ , the dynamic change process of bubble is shown in Figure 16. It also can be seen from the figure that when the copper tube intersects at  $t=0$  ms, it emits strong light and begins to form a bubble. At  $t=0.542$  ms, as the bubble expands, the upper end of the bubble begins to be connected to the hemispheric target. At  $t=1.042$  ms, the bubble continues to expand, and the lower part of the bubble is in a sphere-like shape, which may be due to the reason that the liquid velocity near hemispheric target is less than that far away from the wall. Therefore, the upper end of the bubble is relatively straight. At  $t=1.791$  ms, it can be seen that, with the passage of time, the upper end of the bubble has partially wrapped around the bottom of the hemispheric target surface and expanded further, while the lower part of the bubble is still spherical. At  $t=2.833$  ms, the bubble expands to the maximum volume in the first cycle, and the bubble surrounds the bottom of the hemispheric target. With the bubble shrinking, at  $t=5.541$  ms, the bubble is in an oval-like shape due to the acceleration of bubble shrinkage along the hemispheric target surface. At  $t=5.999$  ms, the oval bubble continues to shrink and appears to be in a slender form. At  $t=6.124$  ms, the bubble collapses to the smallest volume state, and we regard it as the end time of the first stage of bubble pulsation. At this time, the water jet points to the hemisphere target and acts directly on the hemispheric target. At  $t=6.499$  ms, the bubble has entered the expansion stage of the second cycle. Different from the inverted mushroom-like bubble, there is only a small amount of bubble separation and bubble shedding. The bubble is hemispherical and is wrapped around the hemispheric target surface with the passage of time. At  $t=7.499$  ms, the bubble expands to the maximum volume state again. At  $t=9.416$  ms, as the bubble continues to shrink, a small bulge appears at the bottom of bubble. At  $t=9.957$  ms, the bubble collapses to the minimum volume.

By the use of the Hopkinson bar, we recorded and analyzed the bubble load characteristics, as shown in Figure 17. When the bubble collapses in the first cycle, the bubble load has one single peak. When there is a peak load in  $t=6.173$  ms, compared with the bubble dynamics in Figure 16 at  $t=6.124$  ms, it is found that the corresponding load is bubble collapse load  $P_{c-1}$ , and its peak value is 42.3 MPa. When the bubble collapses in the second cycle, the bubble load has bimodal characteristics. When  $t$  is 9.998 ms and 10.01 ms, there are two load peaks. Compared with the bubble dynamics in Figure 16 at  $t=9.957$  ms, it is found that the corresponding loads are bubble collapse load  $P_{c-2}$  and water jet load  $P_{j-2}$ , whose peak values are 29.66 MPa and 22.74 MPa. It is found that the peak value of bubble load decreases obviously in the second cycle.

It is found based on statistical analysis that when the value of the dimensionless distance parameter  $\gamma$  is between 0.67 and 0.83, it has similar bubble shape and load characteristics. Therefore, in order to facilitate the analysis with

different  $\gamma$ , it is divided into oval bubble as type II. As shown in Figure 18, the bubble morphology can be described as follows. In the expansion stage of the first cycle, the electric-spark-generated bubble will expand in the shape of sphere. Due to the influence of boundary conditions, the upper part of the bubble will partially wrap around the hemispheric target when it expands to the maximum. During the first cycle of bubble shrinking, bubbles contract in the form of oval bubble. At this point, a peak pressure is measured by Hopkinson bar, which is the bubble collapse load  $P_{c-1}$  in the first cycle. The bubble expands in a hemispherical shape during the expansion stage of the second cycle, and the bubble surrounds the hemispheric target. In the shrinking stage of the second cycle, the top of hemispherical bubble is connected to the hemispheric target, and a small bulge will appear at the bottom of bubble. In the collapse stage of the second cycle, bubbles will form a jet acting on hemispheric target. At this point, two pressure peaks are also measured by Hopkinson bar, which are bubble collapse load  $P_{c-2}$  and water jet load  $P_{j-2}$  within the second cycle. As mentioned above, there is a pressure load peak value in the first cycle and two pressure load peaks in the second cycle in type II.

**3.3. Drop-Shaped Bubble (Type III).** For the case of  $\gamma=1.17$ , the dynamic change process of bubble is shown in Figure 19. As can be seen from the figure, at  $t=0.875$  ms, the bubble expands in a spherical manner. Because the intersection of the copper tube is far from the bottom of the hemispheric target, the top of the bubble does not contact with the hemispheric target. With the bubble expansion, the bubble volume increases gradually, while it does not contact with the bottom of the hemispheric target. At  $t=3.583$  ms, the bubble expands spherically to the maximum volume in the first cycle. However, different from the two bubble types mentioned above, there is still a certain distance between the top of the bubble and the bottom of the hemispheric target. With the bubble shrinking, at  $t=5.04$  ms, the drop-shaped bubble appears due to the attraction of hemispheric target surface. At  $t=5.499$  ms, the characteristics of the drop-shaped bubble are more obvious, and as the bubble shrinks, the top of the bubble becomes sharper. When the bubble collapses to the smallest volume at  $t=6.124$  ms, it is used as the end time of the first stage of bubble pulsation. During the collapse of the bubble, the bubble is elongated in the direction of the symmetry axis due to the wall attraction. At  $t=6.208$  ms, it means that the bubble begins to expand in the second cycle and an obvious upward water jet can be seen. At  $t=6.791$  ms, with the bubble expansion, the upper part of the bubble expands in a spherical shape and gradually connects to the hemispheric target. Similar to the oval bubble, at this time, a small bulge at the bottom of the bubble appears. At  $t=8.124$  ms, the expansion of bubble in the second cycle reaches the maximum volume, and the top of the bubble is partially wrapped around the bottom of the hemispheric target. At  $t=9.749$  ms, this is the shrinking stage of bubbles in the second cycle. At  $t=9.999$  ms, the bubble collapses and contracts to the smallest volume and this is the end time of

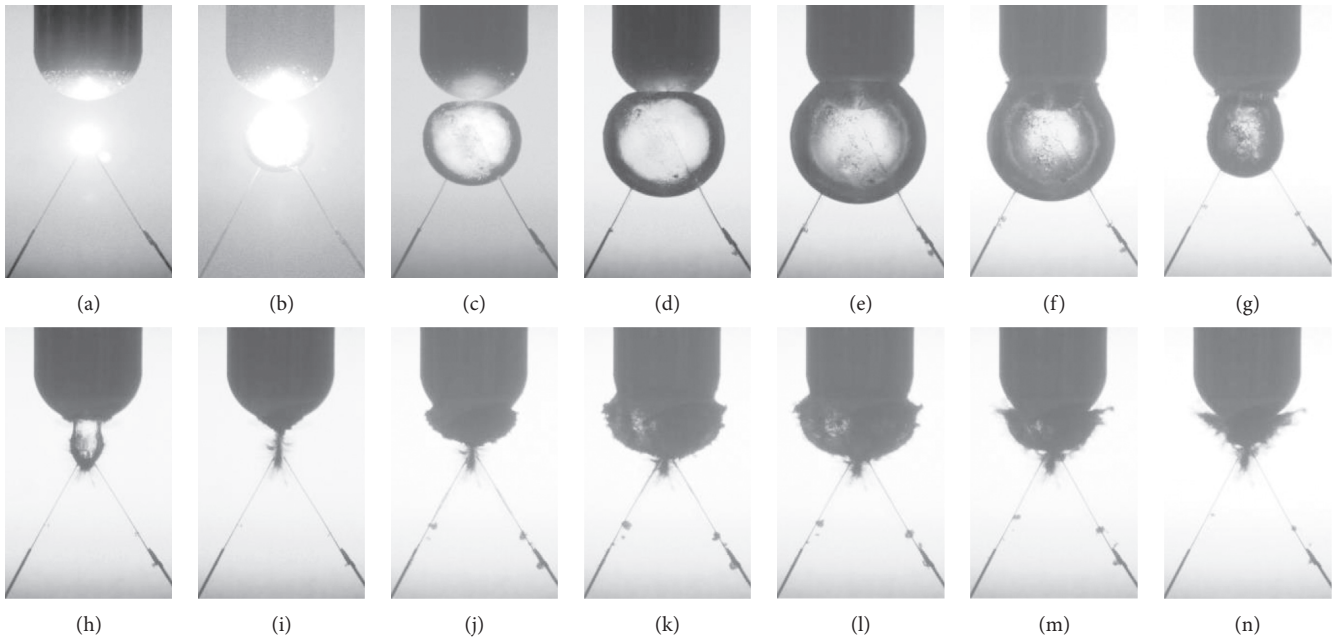


FIGURE 16: Bubble dynamics under the influence of hemispheric boundary for  $\gamma = 0.67$ . (a) 0.000 ms. (b) 0.542 ms. (c) 1.024 ms. (d) 1.791 ms. (e) 2.833 ms. (f) 4.125. (g) 5.541 ms. (h) 5.999 ms. (i) 6.124 ms. (j) 6.499 ms. (k) 7.499 ms. (l) 8.124 ms. (m) 9.416 ms. (n) 9.957 ms.

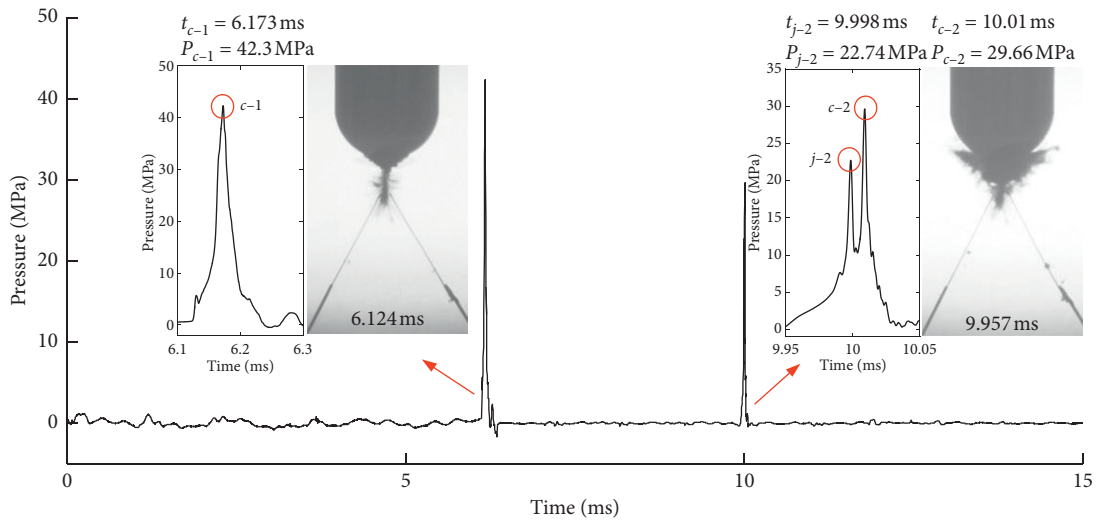


FIGURE 17: Pressure-time diagram of the first and second cycles of the electric-spark-generated bubble load for  $\gamma = 0.67$ .

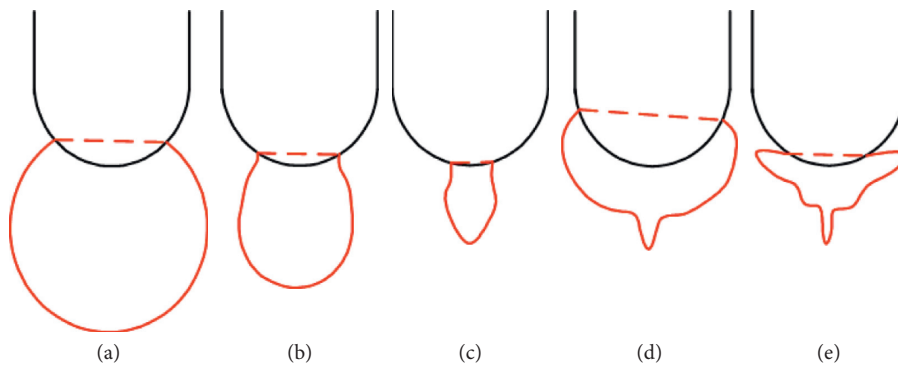


FIGURE 18: Diagram of oval bubble morphological characteristics. (a) First maximum volume. (b) Oval bubble. (c) Oval bubble continues to shrink. (d) Second maximum volume. (e) Second minimum volume.

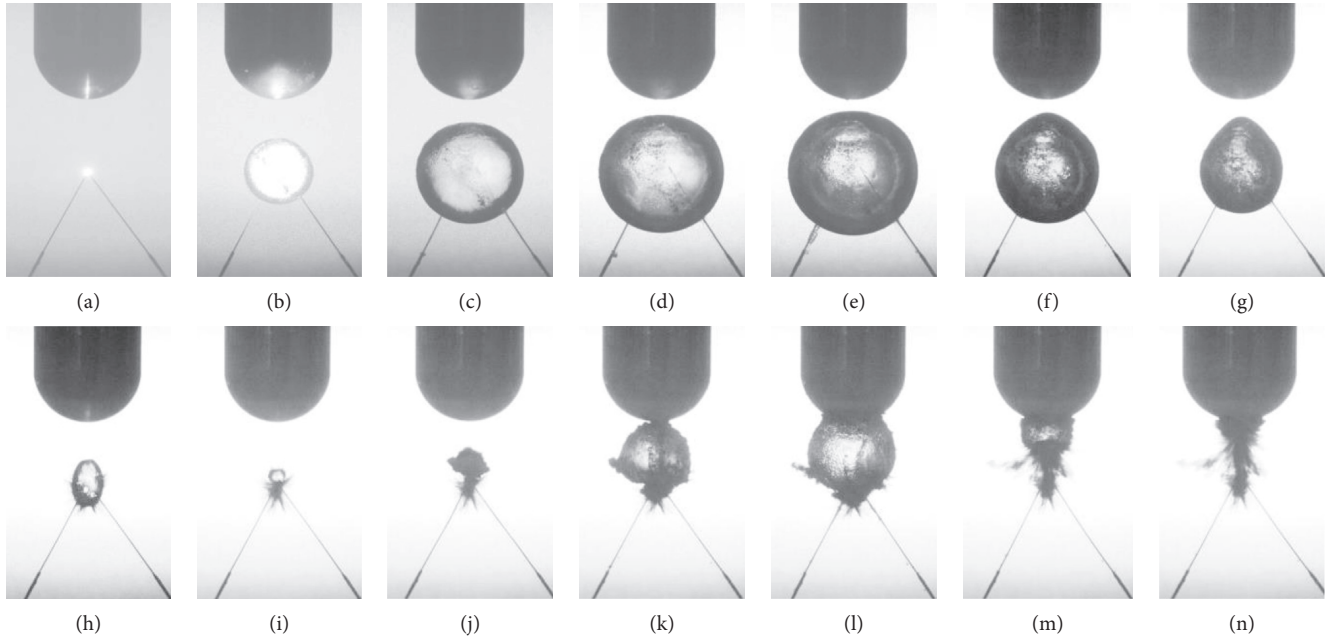


FIGURE 19: Diagram of bubble dynamics under the influence of hemispheric boundary for  $\gamma = 1.17$ . (a) 0.333 ms. (b) 0.875 ms. (c) 1.666 ms. (d) 2.500 ms. (e) 3.583 ms. (f) 5.041 ms. (g) 5.499 ms. (h) 6.041 ms. (i) 6.124 ms. (j) 6.208 ms. (k) 6.791 ms. (l) 8.124 ms. (m) 9.749 ms. (n) 9.999 ms.

bubble pulsation in the second cycle. At this time, the collapse moment can also be clearly observed, and an upward water jet is produced.

By the use of Hopkinson bar, the load characteristics of bubble are analyzed in Figure 20. When the bubble collapses in the first period, the bubble load has bimodal characteristics. When  $t$  is 6.199 ms and 6.213 ms, there are two load peaks. Compared with bubble morphological characteristic diagram in Figure 19 ( $t = 6.124$  ms), it is found that the corresponding loads are bubble collapse load  $P_{c-1}$  and water jet load  $P_{j-1}$ , whose peak values are 15.7 MPa and 10.64 MPa. During the second cycle of collapse stage of the bubble, we also can observe that the bubble load has bimodal characteristics. At  $t = 10.05$  ms, there is a peak load. Compared with the bubble morphology characteristic diagram in Figure 19 ( $t = 9.999$  ms), it is found that the corresponding loads are bubble collapse load  $P_{c-2}$  and water jet load  $P_{j-2}$ , whose peaks are 30.27 MPa and 26.81 MPa. The peak of bubble load is obviously higher in the second cycle, which is related to the relative position of the hemispheric target plate when the bubble collapses.

When  $\gamma = 1.17$ , after the collapse of the bubble in the first cycle, the bubble is sucked by the wall above it vertically, which causes the bubble to move vertically up during the second cycle of “expansion-contraction-collapse” (shown in Figure 19). This displacement makes the distance between the bubble collapse position and the bottom of the Hopkinson bar in the second cycle be less than the distance of first cycle. The shorter measurement distance will make the wall pressure load value measured by Hopkinson bar become larger. This is why the peak pressure in the second cycle shown in Figure 20 is more than the peak pressure in the first cycle.

It is found based on statistical analysis that when the value of the dimensionless distance parameter  $\gamma$  is between 1.00 and 1.50, it has similar bubble shape and load characteristics. Therefore, in order to facilitate the analysis under different  $\gamma$ , it is converted into drop-like bubble as type III. As shown in Figure 21, the bubble morphology can be described as follows. In the expansion stage of the first cycle, the bubble will expand in the shape of sphere. Because the initiation position is far from the hemispheric target, the bubble is not connected to the hemispheric target when the bubble expands to the maximum. However, because the adsorption of the nearby boundary still exists, the bubble will shrink like a drop-shaped bubble in the first cycle. As the bubble collapses, two peak pressures are measured by Hopkinson bar, which are bubble collapse load  $P_{c-1}$  and water jet load  $P_{j-1}$  in the first cycle. The upper part of the bubble expands in a hemispherical in the expansion stage of the second cycle, and the bubble partially surrounds the hemispheric target. In the shrinking stage of the second cycle of the bubble, bubbles contract in the form of hemispherical bubbles, and the top of hemispherical bubbles is connected to the hemispheric target. At the beginning of the collapse stage of the second cycle, a small bulge at the bottom of the bubble will occur. And a water upward jet acting on the hemispheric boundary forms in the second collapse stage. At this time, two pressure peaks are also measured by Hopkinson bar, which are bubble collapse load  $P_{c-2}$  and water jet load  $P_{j-2}$  in the second cycle.

**3.4. Spherical Bubble (Type IV).** For the case of  $\gamma = 2.00$ , the bubble dynamics are different, as shown in Figure 22. As we can see from the figure, as the bubble expands

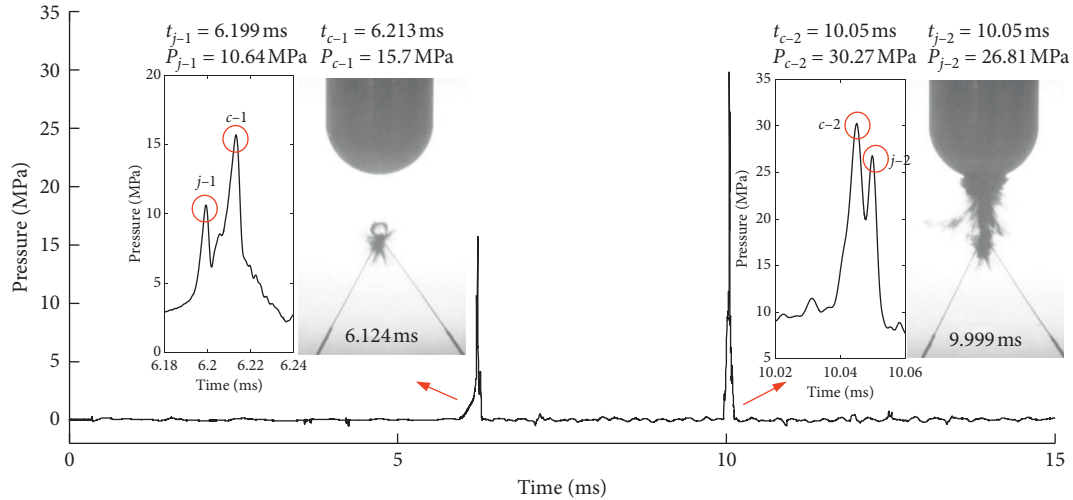


FIGURE 20: Pressure-time diagram of the first and second cycles of the electric-spark-generated bubble load for  $\gamma = 1.17$ .

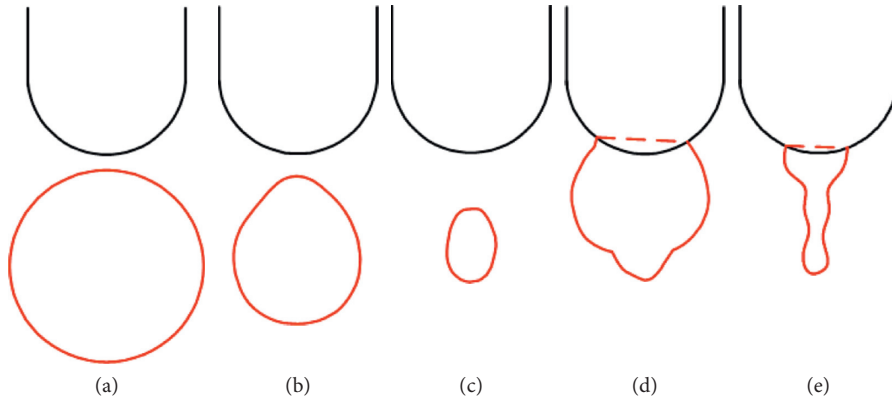


FIGURE 21: Description of drop-like bubble morphological characteristics. (a) First maximum volume. (b) Drop-shaped bubble. (c) First minimum volume. (d) Second maximum volume. (e) Second minimum volume.

( $t = 0 \sim 3.208$  ms), the bubble shows the similar change process as drop-shape bubble (type III); we will not repeat again here. At  $t = 3.208$  ms, the bubble expands spherically to the maximum volume in the first cycle. At  $t = 4.416$  ms, with the bubble shrinking, the bubble shrinkage speed along the hemispheric target surface is accelerated, but the bubble shape is still kept spherical, because the top of the bubble still has a large distance from the bottom of the hemispheric target. So we can conduct that the hemispheric boundary has little impact on the bubble. At  $t = 5.749$  ms, the bubble collapses to the minimum volume. At  $t = 6.249$  ms, it indicates that the bubble begins to expand in the second cycle. As bubble still expands spherically, it reaches the maximum volume in the second cycle at  $t = 7.124$  ms. The bubble collapses to the smallest volume at  $t = 8.457$  ms; it could be seen as the end time of the bubble pulsating the second stage.

The load characteristics of bubble are shown in Figure 23. When the bubble collapses in the first cycle ( $t = 5.636$  ms), the bubble load has one single peak. Compared with bubble morphological characteristic diagram in Figure 22 with  $t = 5.749$  ms, it is found that the corresponding load is bubble collapse load  $P_{c-1}$ , with peak value of 4.924 MPa. When it is

collapse stage of the second cycle of the bubble, the bubble load also has one single peak characteristic. At  $t = 8.018$  ms, it has a peak load; compared with bubble morphological characteristic diagram in Figure 22 with  $t = 8.457$  ms, it is found that the corresponding load is bubble collapse load  $P_{c-2}$ , with peak value of 0.4128 MPa.

It is found based on statistical analysis that when the value of the dimensionless distance parameter  $\gamma$  is between 1.67 and 2.00, it has similar bubble shape and load characteristics. Therefore, in order to facilitate the analysis under different  $\gamma$ , it is divided into spherical bubble as type IV. As shown in Figure 24, the bubble morphology can be described as follows. The bubble expands and contracts in a spherical shape during the first and second cycle. Two bubble pressure peaks are measured by Hopkinson bar, which are the bubble collapse loads  $P_{c-1}$  and  $P_{c-2}$  in the first and second cycle.

#### 4. Bubble Load Characteristics

In this experiment, the wall pressure loads of 12 groups of electric-spark-generated bubble were statistically analyzed, and

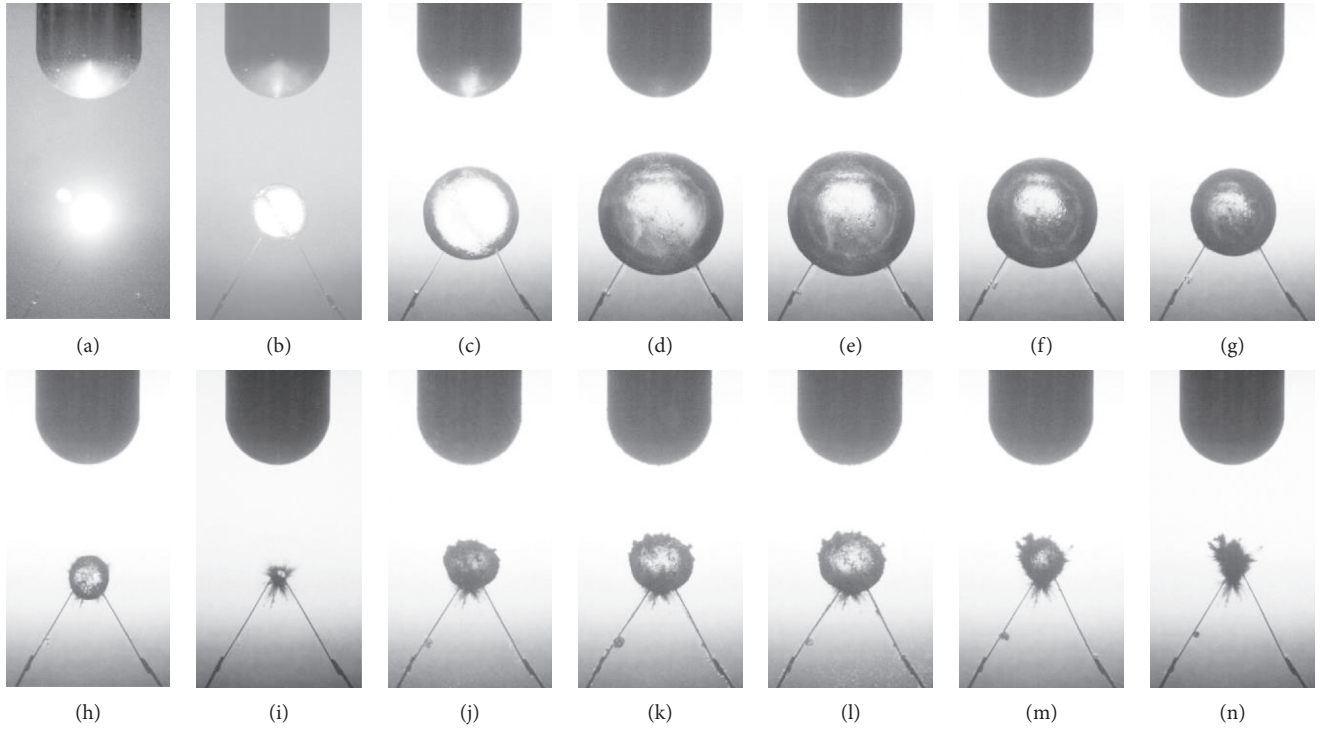


FIGURE 22: Diagram of bubble dynamics under the influence of hemispheric boundary for  $\gamma = 2.0$ : (a) 0.000 ms, (b) 0.416 ms, (c) 1.041 ms, (d) 2.458 ms, (e) 3.208 ms, (f) 4.416 ms, (g) 5.082 ms, (h) 5.624 ms, (i) 5.749 ms, (j) 6.249 ms, (k) 6.707 ms, (l) 7.124 ms, (m) 8.207 ms, and (n) 8.457 ms.

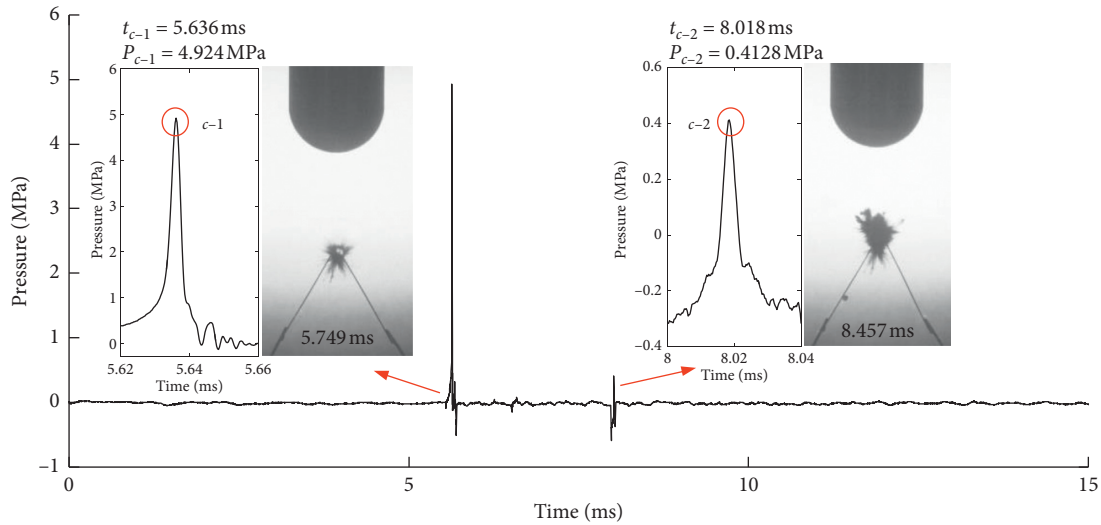


FIGURE 23: Pressure-time diagram of the first and second cycles of the spark-generated bubble load for  $\gamma = 2.0$ .

the distance  $d$  was 5 mm, 10 mm, 15 mm, 20 mm, 25 mm, 30 mm, 35 mm, 40 mm, 45 mm, 50 mm, 55 mm, and 60 mm (i.e.,  $0.17 \leq \gamma \leq 2.00$ ). The details can be found in Appendix. By observing the characteristics of bubble dynamics at different  $\gamma$ , they are divided into four categories, that is, type I, inverted mushroom-like bubble (i.e.,  $0.17 \leq \gamma \leq 0.5$ ), type II, oval bubble (i.e.,  $0.67 \leq \gamma \leq 0.83$ ), type III, drop-shaped bubble (i.e.,

$1.00 \leq \gamma \leq 1.50$ ), and type IV, spherical bubble (i.e.,  $1.67 \leq \gamma \leq 2.00$ ).

According to the records from the Hopkinson bar, it is found that the peak of the wall pressure load during the first bubble collapse gradually decreased with the increase of  $\gamma$ , as shown in Figure 25. The bubble dynamics captured by the high-speed camera were combined with the wall pressure

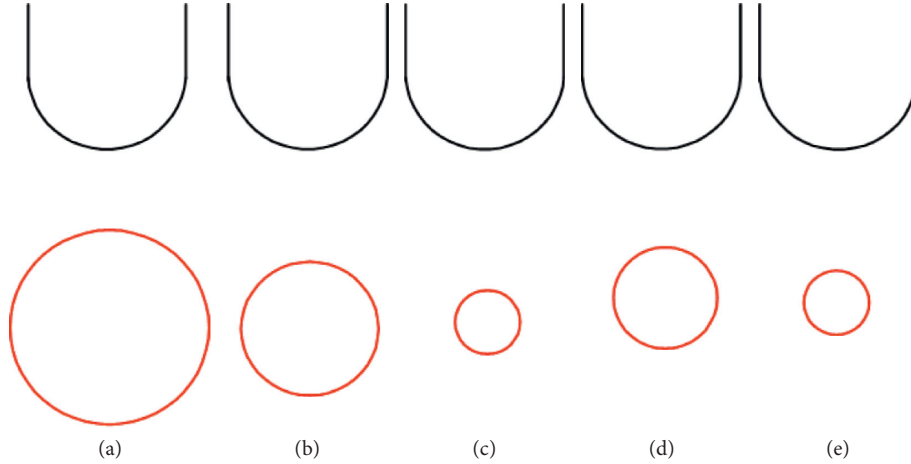


FIGURE 24: Description of spherical bubble morphological characteristics. (a) First maximum volume. (b) Spherical bubble. (c) First minimum volume. (d) Second maximum volume. (e) Second minimum volume.

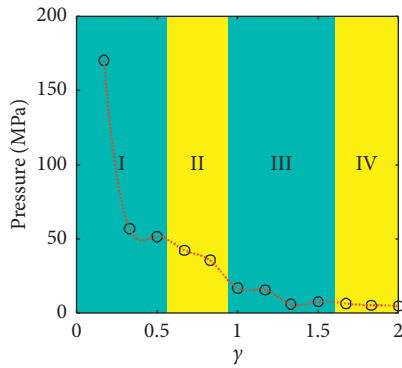


FIGURE 25: Pressure peak of wall pressure variation diagram in the first cycle for  $0.17 \leq \gamma \leq 2.00$ .

load curve measured by Hopkinson bar. We obtain the pulse width data ( $\theta_{c1}$ ) of the collapse load of the first cycle of the bubble when  $0.17 \leq \gamma \leq 2.00$ , and their value ranges are  $0 \text{ ms} \leq \theta_{c1} \leq 0.15 \text{ ms}$ , as shown in Figure 5.

In this experiment, in addition to the wall pressure load produced by the bubble collapse in the first cycle, the wall pressure load produced by the bubble collapse in the second cycle is also measured. When  $0.17 \leq \gamma \leq 0.83$ , the peaks of bubble collapse load are between 20 MPa and 30 MPa in the second cycle. When  $1.00 \leq \gamma \leq 2.00$ , the wall pressure load in the collapse of the bubble is gradually reduced with the increase of  $\gamma$ . When  $\gamma = 1.00$ , after the collapse of the bubble in the first cycle, the bubble is sucked by the wall above it vertically, which causes the bubble to move vertically up during the second cycle. This displacement makes the distance between the bubble collapse position and the bottom of the Hopkinson bar in the second cycle be less than the distance of first cycle. The change in the pressure peak of the bubble collapse load in the second cycle is shown in Figure 26.

The bubble dynamics captured by the high-speed camera were combined with the wall pressure load curve measured

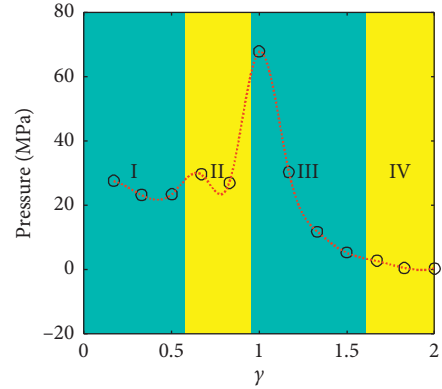


FIGURE 26: Pressure peak of wall pressure variation diagram in the second cycle for  $0.17 \leq \gamma \leq 2.00$ .

by Hopkinson bar. We obtain the pulse width data ( $\theta_{c2}$ ) of the collapse load of the second cycle of the bubble when  $0.17 \leq \gamma \leq 2.00$ , and their value ranges are  $0 \text{ ms} \leq \theta_{c2} \leq 0.15 \text{ ms}$ , as shown in Figure 5.

## 5. Conclusion

In this paper, an electric-spark-generated bubble is obtained with a discharge of 400 V. The whole process of the bubble from the expansion to the collapse is captured by the high-speed camera, and the bubble collapse pressure load is measured by HPB. Based on this, the impact properties of an electric-spark-generated bubble acting on the hemispheric boundary are studied. The following important conclusions are obtained:

- (1) The pressure waveform and peak values measured with the Hopkinson bar agree well with those measured by the pressure transducer, which indicates that the data of the pressure loading of the

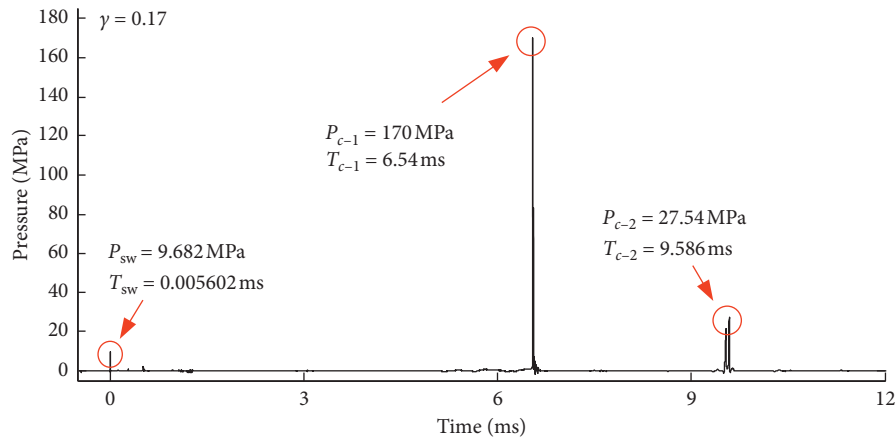


FIGURE 27: Pressure-time diagram of the first and second cycles of the spark-generated bubble load for  $\gamma = 0.17$ .

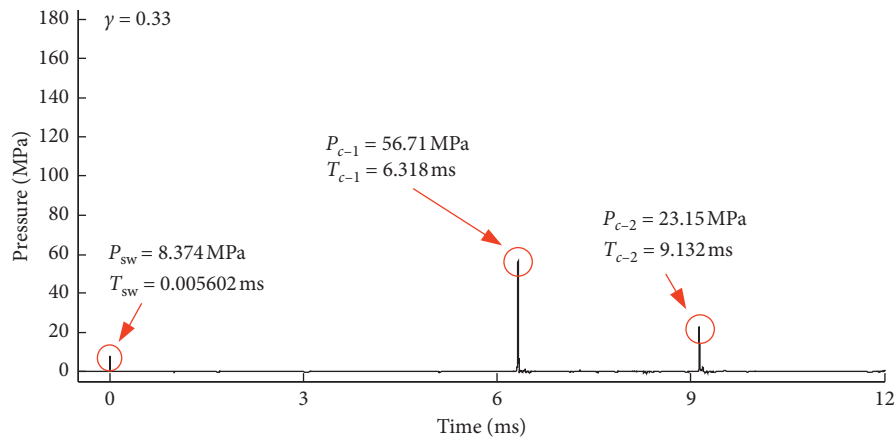


FIGURE 28: Pressure-time diagram of the first and second cycles of the spark-generated bubble load for  $\gamma = 0.33$ .

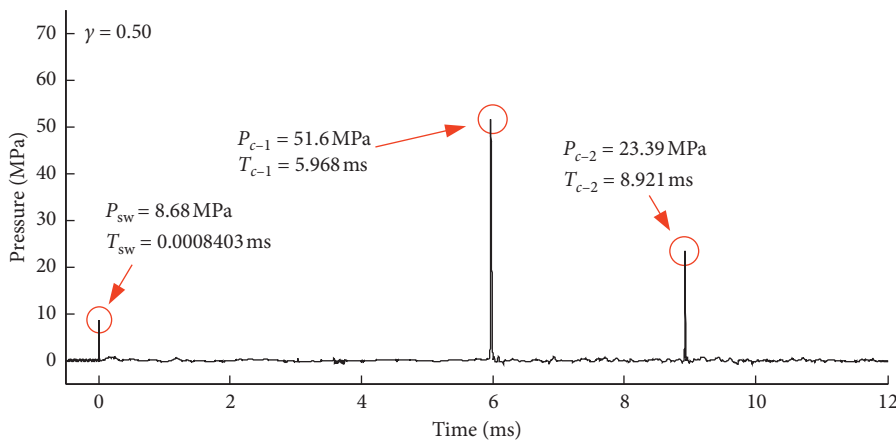


FIGURE 29: Pressure-time diagram of the first and second cycles of the spark-generated bubble load for  $\gamma = 0.50$ .

bubble collapse measured by the Hopkinson bar are valid.

(2) The dimensionless distance ( $\gamma$ ) between bubble and hemispheric boundary has an important influence on the morphology and load characteristics of

bubble. When  $0.17 \leq \gamma \leq 0.5$ , the inverted mushroom-like bubble will be generated at this time. When  $0.67 \leq \gamma \leq 0.83$ , oval bubble will be produced, and collapse loads will be produced in the first cycle and collapse load and jet loads in the second cycle.

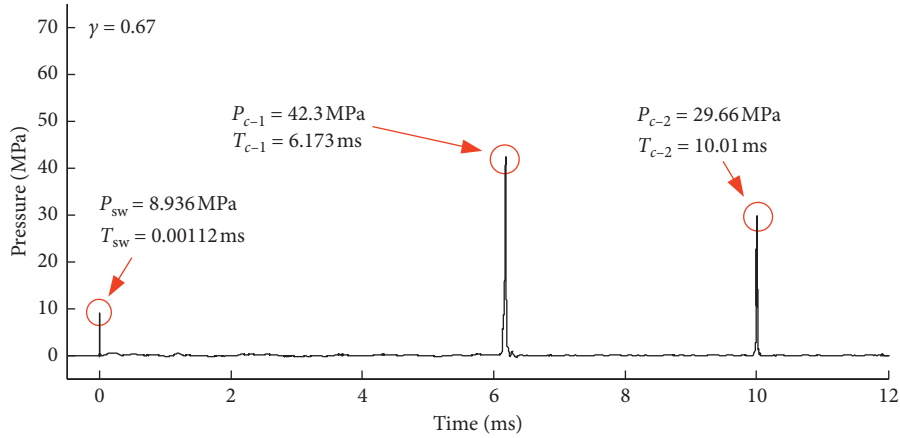


FIGURE 30: Pressure-time diagram of the first and second cycles of the spark-generated bubble load for  $\gamma = 0.67$ .

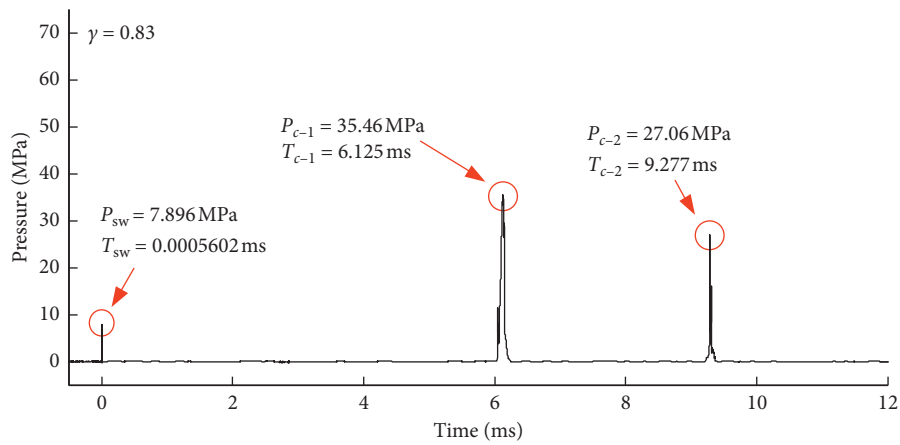


FIGURE 31: Pressure-time diagram of the first and second cycles of the spark-generated bubble load for  $\gamma = 0.83$ .

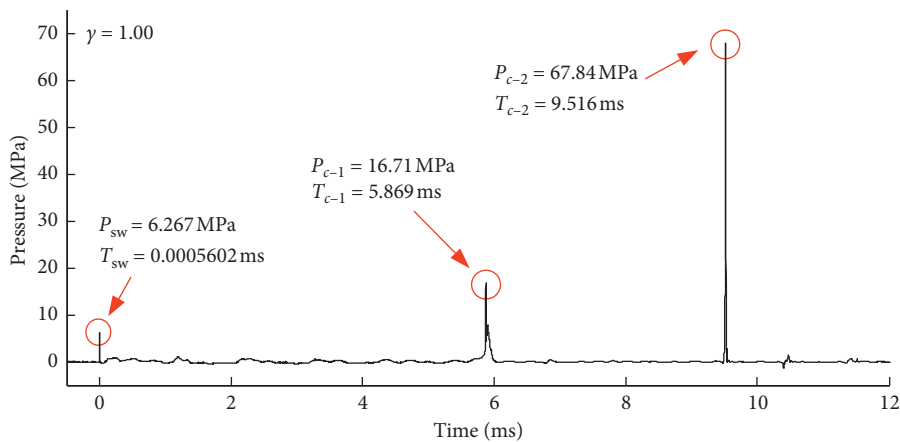


FIGURE 32: Pressure-time diagram of the first and second cycles of the spark-generated bubble load for  $\gamma = 1.00$ .

When  $1.00 \leq \gamma \leq 1.50$ , drop-shaped bubble will be produced, and there will be collapse load and jet load in both the first cycle and the second cycle. When  $1.50 \leq \gamma \leq 2.00$ , there will be spherical bubble, which

only has collapse load in the first cycle and the second cycle.

(3) With regard to the wall pressure loading generated by bubbles in the collapse stage, the peak of wall

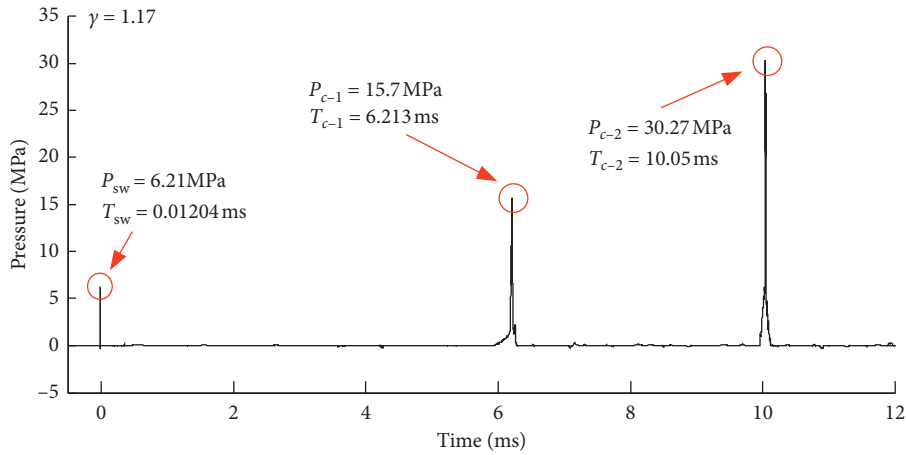


FIGURE 33: Pressure-time diagram of the first and second cycles of the spark-generated bubble load for  $\gamma = 1.17$ .

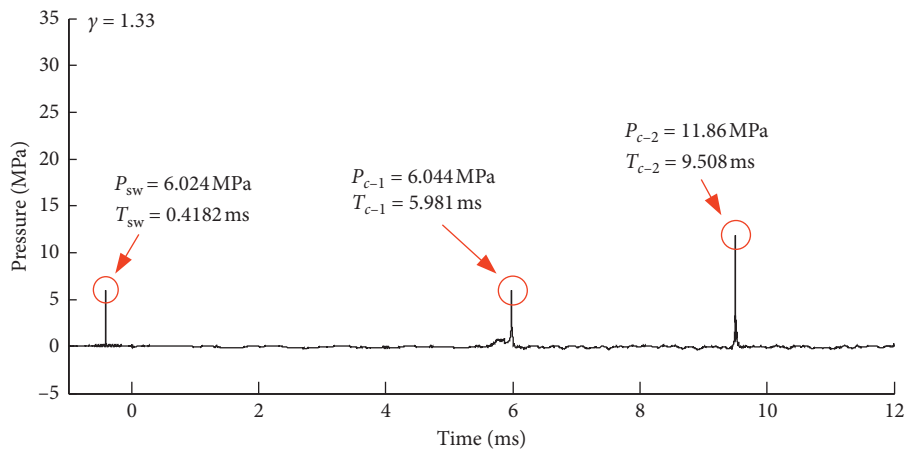


FIGURE 34: Pressure-time diagram of the first and second cycles of the spark-generated bubble load for  $\gamma = 1.33$ .

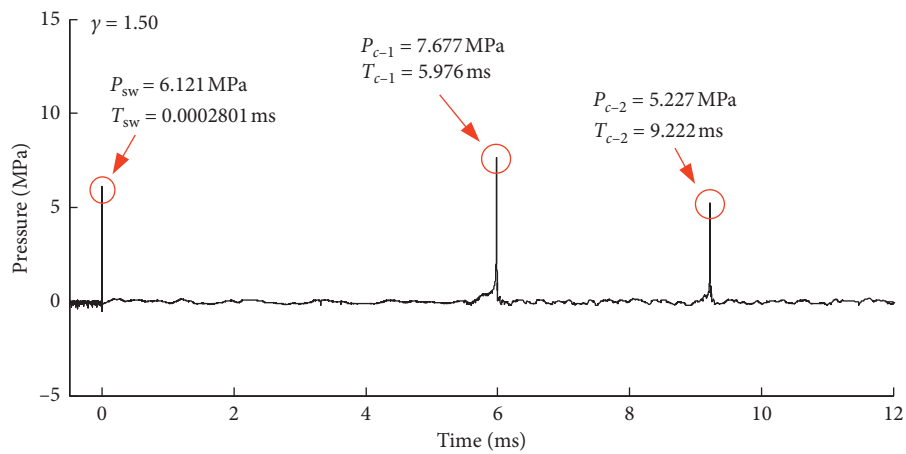


FIGURE 35: Pressure-time diagram of the first and second cycles of the spark-generated bubble load for  $\gamma = 1.50$ .

pressure load decreases with the increase of  $\gamma$  when the bubble collapses for the first cycle. For the wall pressure load caused by the second collapse,

sometimes load abnormalities occur. For example,  $1.00 \leq \gamma \leq 1.33$ . This is because, after the collapse of the bubble in the first cycle, the bubble is sucked by

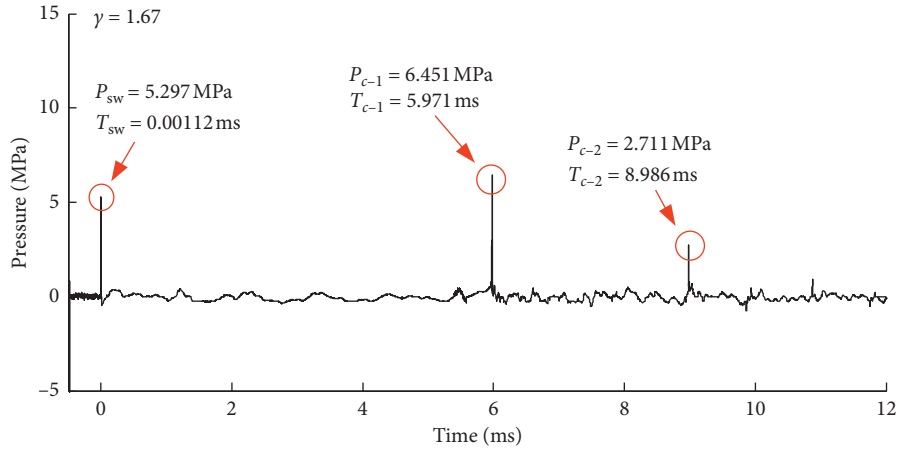


FIGURE 36: Pressure-time diagram of the first and second cycles of the spark-generated bubble load for  $\gamma = 1.67$ .

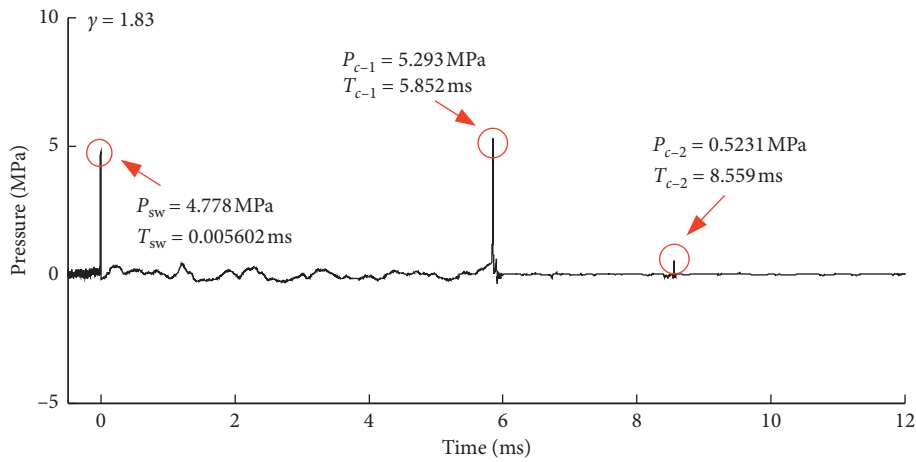


FIGURE 37: Pressure-time diagram of the first and second cycles of the spark-generated bubble load for  $\gamma = 1.83$ .

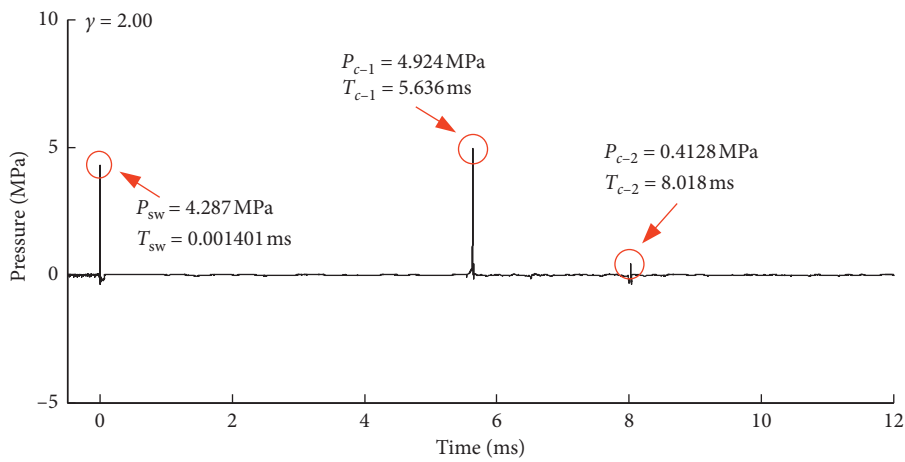


FIGURE 38: Pressure-time diagram of the first and second cycles of the spark-generated bubble load for  $\gamma = 2.00$ .

the wall above it vertically, which causes the bubble to move vertically up during the second cycle. This displacement makes the distance between the bubble collapse position and the bottom of the Hopkinson bar

in the second cycle be less than the distance of first cycle. The shorter measurement distance will make the wall pressure load value measured by Hopkinson bar larger. Therefore, when  $0.17 \leq \gamma \leq 0.83$ , the load produced by

bubble collapse fluctuates between 20 MPa and 30 MPa. The load of  $\gamma = 1.00$  is greater than  $\gamma = 0.83$ . Then, when  $1.00 \leq \gamma \leq 2.00$ , the wall pressure load decreases with the increase of  $\gamma$ .

It is worth mentioning that the conclusion in this research has certain guiding significance for studying the damage characteristics of the bubble under the boundary with different curvatures. For further study, this experimental system can be used to study the bubble dynamics and the pressure mechanics on the boundary with different curvatures.

## Appendix

Wall Pressure Load Curves under Different  $\gamma$  Figures 27–38

## Data Availability

Data present in this paper are available upon request from the corresponding author by e-mail.

## Additional Points

*Highlight.* (i) Firstly, validation of new measurement results of wall pressure based on HPB is done by using the experimental results from pressure transducer. (ii) Secondly, a new measurement based on HPB is used to investigate the wall pressure generated by the electric-spark-generated bubble collapse below the bottom of the hemispherical boundary. (iii) Lastly, the obtained experimental results near the hemispheric boundary are classified according to bubble dynamics and the pressure mechanics.

## Conflicts of Interest

The authors declare that there are no conflicts of interest regarding the publication of this paper.

## Acknowledgments

The authors gratefully acknowledge the financial support provided by the National Natural Science Foundation of China (no. 51779056, no. 51679056, and no. U1430236), Natural Science Foundation of Heilongjiang Province of China (E2016024), Science Foundation of Heilongjiang Province (QC201852), and the Fundamental Research Funds for the Central Universities (HEUCFP201742).

## References

- [1] G. L. Chahine, "Experimental and asymptotic study of nonspherical bubble collapse," *Mechanics and Physics of Bubbles in Liquids*, vol. 38, no. 1, pp. 187–197, 1982.
- [2] G. L. Chahine, "Modeling of scavitation dynamics and interaction with material," in *Advanced Experimental and Numerical Techniques for Cavitation Erosion Prediction*, pp. 123–161, Springer, Berlin, Germany, 2014.
- [3] J. Luo, W. Xu, J. Deng, Y. Zhai, and Q. Zhang, "Experimental study on the impact characteristics of cavitation bubble collapse on a wall," *Water*, vol. 10, no. 9, 2018.
- [4] O. Supponen, D. Obreschkow, and M. Farhat, "Rebounds of deformed cavitation bubbles," *Physical Review Fluids*, vol. 3, no. 10, 2018.
- [5] G. L. Chahine, A. Kapahi, J. K. Choi, and C. T. Hsiao, "Modeling of surface cleaning by cavitation bubble dynamics and collapse," *Ultrasonics Sonochemistry*, vol. 29, pp. 528–549, 2015.
- [6] A. Philipp and W. Lauterborn, "Cavitation erosion by single laser-produced bubbles," *Journal of Fluid Mechanics*, vol. 361, pp. 75–116, 1998.
- [7] G. L. Chahine, J. P. Franc, and A. Karimi, "Cavitation and cavitation erosion," in *Advanced Experimental and Numerical Techniques for Cavitation Erosion Prediction*, pp. 3–20, Springer, Berlin, Germany, 2014.
- [8] P. Cui, A. M. Zhang, and S. P. Wang, "Small-charge underwater explosion bubble experiments under various boundary conditions," *Physics of Fluids*, vol. 28, no. 11, 2016.
- [9] R. P. Tong, W. P. Schiffers, S. J. Shaw, J. R. Blake, and D. C. Emmony, "The role of "splashing" in the collapse of a laser-generated cavity near a rigid boundary," *Journal of Fluid Mechanics*, vol. 380, pp. 339–361, 1999.
- [10] X. Cui, X. Yao, and Y. Chen, "A lab-scale experiment approach to the measurement of wall pressure from near-field under water explosions by a hopkinson bar," *Shock and Vibration*, vol. 2018, Article ID 8273469, 15 pages, 2018.
- [11] S. Li, A. M. Zhang, and X. L. Yao, "Experimental and numerical study on the dynamic pressure caused by the bubble jet," *Journal of Physics: Conference Series*, vol. 656, Article ID 012025, 2015.
- [12] S. Li, S. P. Wang, and A. M. Zhang, "Bubble jet impact on a rigid wall of different stand-off parameters," *IOP Conference Series: Materials Science and Engineering*, vol. 72, no. 2, Article ID 022010, 2015.
- [13] S. Li, Y.-b. Li, and A.-m. Zhang, "Numerical analysis of the bubble jet impact on a rigid wall," *Applied Ocean Research*, vol. 50, pp. 227–236, 2015.
- [14] Y. Chen, X. Yao, and X. Cui, "A numerical and experimental study of wall pressure caused by an underwater explosion bubble," *Mathematical Problems in Engineering*, vol. 2018, Article ID 6139510, 10 pages, 2018.
- [15] Y. Tomita, P. B. Robinson, R. P. Tong, and J. R. Blake, "Growth and collapse of cavitation bubbles near a curved rigid boundary," *Journal of Fluid Mechanics*, vol. 466, pp. 259–283, 2002.
- [16] P. Cui, A.-m. Zhang, S.-p. Wang, and Q.-x. Wang, "Experimental investigation of bubble dynamics near the bilge with a circular opening," *Applied Ocean Research*, vol. 41, pp. 65–75, 2013.
- [17] S. Li, B. C. Khoo, A.-M. Zhang, and S. Wang, "Bubble-sphere interaction beneath a free surface," *Ocean Engineering*, vol. 169, pp. 469–483, 2018.
- [18] S. Li, A. M. Zhang, R. Han, and Q. Ma, "3D full coupling model for strong interaction between a pulsating bubble and a movable sphere," *Journal of Computational Physics*, vol. 392, pp. 713–731, 2019.
- [19] S. Li, A. M. Zhang, and R. Han, "Letter: counter-jet formation of an expanding bubble near a curved elastic boundary," *Physics of Fluids*, vol. 30, no. 12, 2018.
- [20] S. D. Clarke, S. D. Fay, J. A. Warren, A. Tyas, S. E. Rigby, and I. Elgy, "A large scale experimental approach to the measurement of spatially and temporally localised loading from the detonation of shallow-buried explosives," *Measurement Science and Technology*, vol. 26, no. 1, Article ID 015001, 2014.

- [21] S. D. Clarke, S. D. Fay, J. A. Warren et al., "Geotechnical causes for variations in output measured from shallow buried charges," *International Journal of Impact Engineering*, vol. 86, pp. 274–283, 2015.
- [22] S. E. Rigby, S. D. Fay, S. D. Clarke et al., "Measuring spatial pressure distribution from explosives buried in dry Leighton Buzzard sand," *International Journal of Impact Engineering*, vol. 96, pp. 89–104, 2016.
- [23] X. Yao, K. Guo, Y. Chen, and X. Cui, "A new experimental methodology to assess the wall pressure generated by a high-voltage underwater Spark-generated bubble," *Results in Physics*, vol. 12, pp. 571–574, 2019.
- [24] X. Yao, X. Cui, K. Guo, and Y. Chen, "An experimental approach to the measurement of wall pressure generated by an underwater spark-generated bubble by a hopkinson bar," *Shock and Vibration*, vol. 2019, Article ID 5341317, pp. 1–14, 2019.
- [25] A. Shima, K. Takayama, Y. Tomita, and N. Ohsawa, "Mechanism OF impact pressure generation from spark-generated bubble collapse near a wall," *AIAA Journal*, vol. 21, no. 1, pp. 55–59, 1983.
- [26] S. W. Fong, D. Adhikari, E. Klaseboer, and B. C. Khoo, "Interactions of multiple spark-generated bubbles with phase differences," *Experiments in Fluids*, vol. 46, no. 4, pp. 705–724, 2009.
- [27] A. Jayaprakash, G. Chahine, and C. T. Hsiao, "Numerical and experimental study of the interaction of a spark-generated bubble and a vertical wall," in *Proceedings of the ASME International Mechanical Engineering Congress and Exposition*, Pittsburgh, PA, USA, November 2010.
- [28] A. Dadvand, M. Dawoodian, B. C. Khoo, and R. Esmaily, "Spark-generated bubble collapse near or inside a circular aperture and the ensuing vortex ring and droplet formation," *Acta Mechanica Sinica*, vol. 29, no. 5, pp. 657–666, 2013.
- [29] J. Luo, W.-l. Xu, Z.-p. Niu, S.-j. Luo, and Q.-w. Zheng, "Experimental study of the interaction between the spark-induced cavitation bubble and the air bubble," *Journal of Hydrodynamics*, vol. 25, no. 6, pp. 895–902, 2013.
- [30] S. Zhang, S. P. Wang, and A. M. Zhang, "Experimental study on the interaction between bubble and free surface using a high-voltage spark generator," *Physics of Fluids*, vol. 28, no. 3, 2016.